Dynamic stabilization of ablative Rayleigh-Taylor instability in the presence of a temporally modulated laser pulse

K. G. Zhao,[1,2,3] Z. Y. Li,[2] L. F. Wang,[2,3,*] Z. H. Di,[2,4] C. Xue,[2] H. Zhang,[1] J. F. Wu,[2] W. H. Ye,[2,3] C. T. Zhou,[1,3] Y. K. Ding,[2,3] W. Y. Zhang,[2,3] and X. T. He[1,2,3]

[1]*Shenzhen Key Laboratory of Ultraintense Laser and Advanced Material Technology, Center for Intense Laser Application Technology, and College of Engineering Physics, Shenzhen Technology University, Shenzhen 518118, People's Republic of China*

[2]*Institute of Applied Physics and Computational Mathematics, Beijing 100094, People's Republic of China*

[3]*HEDPS, Center for Applied Physics and Technology, Peking University, Beijing 100871, People's Republic of China*

[4]*State Key Laboratory for Geomechanics and Deep Underground Engineering, China University of Mining and Technology, Beijing 100083, People's Republic of China*

(Received 18 September 2023; accepted 2 February 2024; published 26 February 2024)

This paper presents a numeric study of the dynamic stabilization of the ablative Rayleigh-Taylor instability (ARTI) in the presence of a temporally modulated laser pulse. The results show that the specially modulated laser produces a dynamically stabilized configuration near the ablation front. The physical features of the relevant laser-driven parameters in the unperturbed ablative flows have been analyzed to reveal the inherent stability mechanism underlying the dynamically stabilized configuration. A single-mode ARTI for the modulated laser pulse is first compared with that of the unmodulated laser pulse. The results show that the modulated laser stabilizes the surface perturbations and reduces the linear growth rate and enhancement of the cutoff wavelength. For multimode perturbations, the dynamic stabilization effect of the modulated laser pulse contributes to suppress the small-scale structure and reduce the width of the mixing layer. Moreover, the results show that the stabilization effect of the modulated laser pulse decreases as the maximum wavelength increases.

DOI: 10.1103/PhysRevE.109.025213

I. INTRODUCTION

Inertial confinement fusion (ICF) involves high-power lasers or soft x-rays driving the spherical compression of a capsule containing deuterium and tritium as fuel, with the goal being to achieve self-sustaining fusion [1–5]. In the central hot-spot ignition ICF scheme, the driving source heats the shell outer surface of the spherical capsule, causing a low-density plasma to inwardly accelerate the high-density shell [6,7]. During the acceleration phase, perturbations seeded by nonuniform irradiation and surface roughness on the capsules are magnified via the Rayleigh-Taylor instability (RTI) [8,9]. Sufficient growth of the perturbation can cause the dense shell to break up and mix the shell material into the main fuel at a later stage of the implosion [10–12]. The RTI is one of the main challenges to overcome to achieve ignition [13]. During the course of an ICF implosion, the RTI must be reduced to an acceptable level, to improve implosion performance and achieve the desired fusion burning and high gain.

Considerable research has been devoted to reduce the growth of the ablative RTI (ARTI) in laser-driven targets. Previous studies show that mass ablation is caused by heat flux leaving the unstable interface [14–21], which indicates that mass ablation tends to stabilize the ARTI. The growth rate of the ARTI derived by Bodner and Takabe [14,15], $\gamma = \alpha\sqrt{kg} - \beta k V_a$, is generally consistent with the experimental results [22], where $k = 2\pi/\lambda$ is the perturbation wave number, g is the acceleration, and $V_a = \dot{m}/\rho_h$ is the ablation velocity. The parameters α and β are coefficients that depend on the ablative flow parameters. As predicted by the dispersion relation, Fujioka *et al.* [23] observed that the density profile stabilizes laser-driven targets. Considering the density profile stabilization at the ablation front [17,24,25], the ARTI linear growth rate is $\gamma = \alpha\sqrt{kg/(1+kL_m)} - \beta k V_a$, where $L_m = \min[|\rho/(\partial\rho/\partial x)|]$ is the minimum density gradient scale length at the ablation surface. Ye *et al.* [26] proposed the modified formula for the preheating case.

To improve stability, a wide variety of strategies have been proposed to further suppress the ARTI or/and mitigate the laser imprint on direct-drive ICF implosions. In recent years, efforts have increased with adiabat-shaping techniques, [27] which involve designing the laser pulse with both small pickets [28] and "high-foot" [29] types; these designs stabilize the instability in the ablator. The possible stabilizing mechanisms of nonlocal electron heat transport [30], high-Z-doped target [31], radiation preheating [32], and magnetic field [33,34] affect the evolution of the ARTI. While these physical mechanisms and strategies control the RTI growth to avoid the nonlinear behavior [35,36], amplifications of perturbations seeded by target roughness and laser imprint still threaten the ignition process. For this reason, developing methods to suppress the instability growth could ultimately prove crucial to improving implosion performance in ICF experiments.

Dynamic stabilization driven by the vertical vibration of the ablation front in an ICF scenario has been suggested as a possible stabilization method for mitigating or suppressing

*wang_lifeng@iapcm.ac.cn, lif_wang@pku.edu.cn

the instability growth [37–40]. The dynamic stabilization of the ARTI in ICF targets was first developed in numerical simulations by Boris [37], and later Betti *et al.* developed a linear stability analysis for a sinusoidal modulation of the laser intensity [38]. To gain a deeper insight into the different modulation of the driving acceleration $g(t) = g_0 + b\Gamma(\omega t)$, Piriz *et al.* [39,40] used a simplified theoretical model to obtain the dispersion relations of the dynamic stabilization of the RTI in the ablation front. Here g_0 is the background acceleration, $b\Gamma(\omega t)$ is the local acceleration that oscillates with the frequency ω and amplitude $b = \omega^2 A$ of the modulation acceleration, and A is an amplitude of a harmonic oscillation in the vertical direction at the interface of two fluids. In general, the mass ablation effects of the ARTI in ICF implosions resembles those produced by the viscosity and surface tension in Newtonian fluids [41]. The dynamic stabilization of the RTI in Newtonian fluids has been experimentally demonstrated by applying vertical vibration [42,43], and the analyses of these experiments indicate the importance of viscosity and surface tension in determining the possible stable regions [44–46]. The consistency between the theoretical model and experimental results demonstrates modulating the driving acceleration is a feasible method to dynamically stabilize the RTI.

Although the linear stability analysis accurately predicts the growth rate and the stability region of the dynamically stabilized ARTI, the analytical results are obtained by using the simplest modulation in the acceleration [38–40]. A related but more complicated acceleration for the dynamically stabilized configuration is established near the ablation front when a planar target is irradiated by an appropriately modulated laser. Notably, such a modulated laser pulse plays a significant role in stabilizing the ARTI growth and is feasible at a real laser facility for applications to direct-drive ICF ignition target designs. Another interesting aspect of the dynamically stabilized configuration is that the modulation frequency depends both on compressibility and the response time of the target materials imposed by the oscillating ablation pressure. Therefore, the dynamic stabilization of the modulated laser pulse must be regarded from a broader perspective. Revealing the inherent stability mechanism underlying the dynamically stabilized configuration is of great importance to the success of laser direct-drive ICF ignition.

This work applies a full analysis of the relevant laser-driven parameters in the ablative flow to better understand the dynamic stabilization effect of the modulated laser pulse. The interface is stable only when accelerated from the heavier to the lighter fluid, which is a criterion to reveal the intrinsic stability mechanism of the ablation front. Still, obtaining such physical parameters is essential to present the stabilizing features of the dynamically stabilized configuration. In addition, according to the phenomenology of the nonlinear RTI in the presence of time-varying accelerations [47,48], both experimental and simulated results indicate that the growth and late-time scaling of the nonlinear RTI depend on the temporal acceleration profile $g(t)$. In particular, the periodic modulation of the acceleration field suppresses the turbulent mixing by the classical RTI. To date, the dynamic stabilization of the modulated laser pulse has not been studied beyond the linear regime. Therefore, it is necessary to study the nonlinear dynamics of the multimode ARTI underlying the dynamically stabilized configuration to understand the stabilization effect of the modulated laser pulse in the mixing region.

The remainder of this paper is organized as follows. The mathematical framework and numerical setup are presented in Sec. II. The simulation results are reported in Sec. III, where we analyze the stability features of the unperturbed ablative flow and discuss the dynamic stabilization for single-mode and multimode ARTIs. Finally, the conclusions are given in Sec. IV.

II. NUMERICAL METHODS AND SIMULATION SETUPS

A. Governing equations

This study models the physical system as a two-dimensional (2D) inviscid, single-temperature single fluid with laser energy deposition and the thermal conduction. Not considering radiation, our numerical code is based on an ideal gas equation of state, the governing equations of which are

$$\frac{\partial \rho}{\partial t} + \nabla \cdot (\rho \mathbf{u}) = 0, \tag{1}$$

$$\frac{\partial \rho \mathbf{u}}{\partial t} + \nabla \cdot (\rho \mathbf{u}\mathbf{u}) + \nabla p = 0, \tag{2}$$

$$\frac{\partial E}{\partial t} + \nabla \cdot [(E + p)\mathbf{u}] = \nabla \cdot (\kappa \nabla T) + W_L, \tag{3}$$

where ρ (g/cm^3), $\mathbf{u}$ (cm/μs), and T (MK) are the density, velocity, and temperature, respectively, $p = c_{\rm v}(\gamma_h - 1)\rho T$ is the pressure, $E = c_{\rm v}\rho T + \rho \mathbf{u}\mathbf{u}/2$ is the total energy, $c_{\rm v}$ is the specific heat at constant volume, and γ_h is the specific heat ratio. For the plastic (CH) foil material, $\gamma_h = 5/3$ and $c_{\rm v} = 86.2713$ cm μs^{-2} MK^{-1}.

For intense laser irradiation of planar targets, the laser energy deposition W_L is calculated by using the inverse bremsstrahlung absorption model [49–51]. Together with the heat flux transported by the electron thermal conduction, the electron thermal conductivity coefficient $\kappa = \kappa_0 T^{5/2}$ is calculated by using the classical Spitzer-Härm electron thermal transport model [52]. The one-dimensional (1D) simulation assumes that a planar target is irradiated directly by a laser beam with a wavelength of ~ 351 nm and where the intensity increases linearly to a maximum and then remains constant.

B. Numerical methods

For simplicity, the system of partial differential equations is expressed in the form

$$\mathbf{Q}_t + L\mathbf{Q} = L_v \mathbf{Q} + \mathbf{S}, \tag{4}$$

where the conservative variable $\mathbf{Q} = (\rho, \rho u, \rho v, E)^T$, and u and v are the velocities in the x and y directions, respectively. L and L_v are the spatial differential operators for the first-order (inviscid, nonlinear, hyperbolic) and second-order (linear, parabolic) terms, respectively, and $\mathbf{S}$ is approximated as the bulk-force source term.

The complete simulation code [53], including the hydrodynamic module, the laser energy deposition, and the electron thermal conduction, is designed to solve the governing equations. A finite volume method is used to solve

Eq. (4). The numerical results of $L\mathbf{Q}$ are obtained by solving the approximate Riemann problem [54]. A nonuniform grid is used to reduce the computational load. Grid-moving (target-tracking) technology ensures that the ablation surface is always under the refined-mesh area. Considering the incident and reflection process in an intense laser illumination of planar targets, the source term $\mathbf{S}$ involving the laser energy deposition is calculated by the physical parameters obtained from the hydrodynamic module. A redesigned grid and a parallel partitioning strategy avoids parallel communication and improves the efficiency. When the thermal conductivity coefficient $\kappa \neq 0$, the second-order parabolic term involving the electron thermal conduction is solved by using an implicit iteration method for the large and sparse linear system of equations, which is provided by the HYPRE library in the form of high-performance preconditions and solvers [55]. The second-order accuracy in spatial and temporal discretization is thus determined via numerical methods.

The physical domain is rectangular. The domain length in the laser direction x is $L_x = 1610.8$ μm. For single-mode perturbations, the domain in the transverse direction y is chosen to be periodic with length $L_y = \lambda$, where λ is the perturbation wavelength. The simulation domain in the y direction for multimode perturbations uses $L_y = 150$ μm. Free-stream boundary conditions are imposed at both ends of the domain in the x direction because, for a sufficiently large domain, the flow remains unchanged far from the center of the computational domain. Periodic boundary conditions are imposed on the upper and lower boundaries of the simulation domain in the y direction.

In the simulations presented in Sec. III, the spatially uniform and nonuniform grid points are designed in the transverse and laser directions, respectively. The cell size along the laser direction is finely gridded with $\Delta x = 0.2$ μm over the entire ablation front and the critical density regions, then stretching smoothly to about $\Delta x = 2.0$ μm on either side of the finely gridded region. Properties similar to those of the present numerical grid are used in the laser-matter interaction codes FAST2D and FastRad3D [50,56,57]. Furthermore, the grid ratio $\Delta x/\Delta y$ of our grid distribution ranges from 0.256 to 2.56 in all regions and is similar to the distribution of grids points reported by Gardner *et al.* for growth of the ARTI [58]. For initial multimode perturbations, the number of grid points used in the x and y directions are $N_x = 2760$ and $N_y = 1024$, respectively.

C. Setup of initial conditions

To explore how the specially modulated laser pulse dynamically stabilizes the nonlinear evolution of the ARTI, we must obtain a quasisteady ablative flow in the noninertial reference frame of the accelerating target. More specifically, a 400 μm thick plastic target with a density of 1.0 g/cm^3 [see Fig. 1(a)] is irradiated directly by a laser beam with a wavelength $\sim$ 351 nm and maximum intensity 3.0×10^{14} W/cm^2. The intensity of this laser pulse increases linearly within 4.0 ns and then remains at its maximum value, as plotted in Fig. 1(b). The laser intensity required for the numerical simulation is well within the working range of already existing laboratory apparatuses, which provides an opportunity to answer some

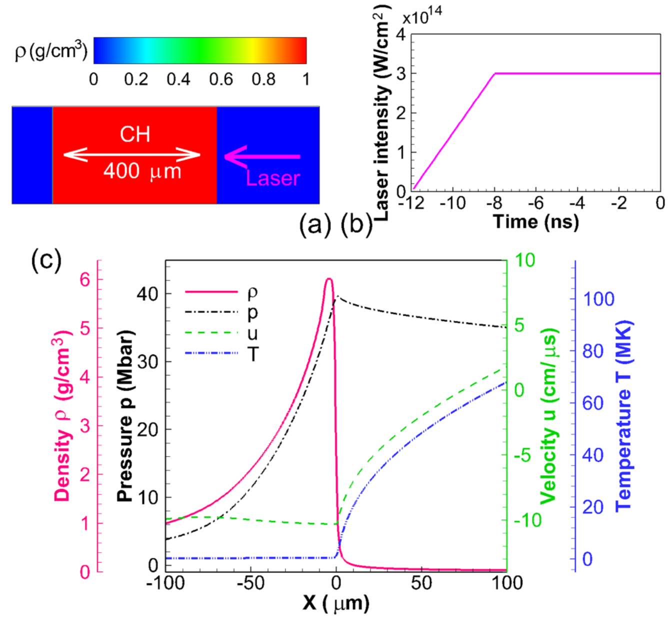

FIG. 1. (a) Schematic of planar target. (b) Profile of laser intensity. (c) Distribution of initial basic flow ($t = 0.0$ ns) along the x axis. The minimum density gradient scale length of the ablation front is about 0.93 μm.

critical questions. For a higher laser intensity (i.e., $\gtrsim 10^{15}$ W/cm^2), we hope to use this laser intensity in future research into ablative flow problems. When the target material is irradiated by this intense laser beam, the ablation front accelerates. The instantaneous acceleration is oscillatory in the early stage and approaches a constant value, which indicates that the quasisteady ablative flow is established in the vicinity of the ablation front (defined as the zone at half-peak density). For the ARTI problem, the ablative flow must be maintained in the quasisteady-acceleration phase.

We have chosen the ablative flow at time 0.0 ns as the initial basic flow for the following simulations. The initial condition of this ablative flow is quasisteady state, which corresponds to a typical acceleration phase of the laser direct-drive target ICF. As shown in Fig. 1(c), the initial ablation front is at $s(t = 0.0 \text{ ns}) \approx 0.0$ μm and the peak density $\rho_h \approx 6.0$ g/cm^3. The pressure driving the dense compressed target comes primarily from removal of the ablated material at the surface of the planar target. Therefore, by adopting the noninertial reference frame of the dense compressed target, the target supported by the low-density plasma of the ablation flow is in the effective gravitational field of the acceleration. Furthermore, the initial velocity of the ablation front in the quasisteady ablative flow is about 10.5 cm/μs due to the target material has been already driven within 12 ns, as shown in Fig. 1(c). Accordingly, we choose this ablative flow as an initial ablative flow. Thereafter the driving acceleration of the ablation front will be constant.

The primitive variables (ρ, u, v, T) of the initial quasisteady ablative flow are perturbed by the interface perturbation. Actually, the perturbations on all relevant interfaces are generally a natural multimode. To investigate the multimode perturbations in the ablative flows generated by unmodulated and modulated laser pulses, the initial perturbations with a continuous spectrum and a random phase are in two dimensions.

III. SIMULATION RESULTS AND DISCUSSION

This section describes the 1D ablative flows and 2D simulation results of the single-mode and multimode ARTIs in a laser-driven planar target. First, we discuss the physical features of the relevant parameters in the unperturbed ablative flow, and reveal the inherent stability mechanism of the specially modulated laser pulse. Second, we describe the dynamic stabilization behaviors of the ARTI with the single-mode perturbation at the ablation surface. Finally, the spatial structure of the ablation surface and the nonlinear dynamics for multimode ARTI are simulated and analyzed to investigate the dynamic stabilization behaviors of the modulated laser pulse in the nonlinear evolution of the system.

A. Stability analysis of the unperturbed ablative flow

Previously published theoretical studies of the dynamic stabilization of the RTI in the ablation front focused on the modulation of the driving acceleration [39,40]. The analysis of the theoretical results indicates that dynamic stabilization depends on the driving waveform, vibration frequency, and oscillation amplitude of the modulation acceleration. More importantly, the driving acceleration involving a Dirac δ function produces the best dynamic stabilization. In our simulations, the laser pulse, specially modulated as a function of time to produce the oscillating ablation pressure, is determined by running multiple simulations. When the unablated material layer ahead of the ablation front is imposed by the oscillating ablation pressure, it exhibits a periodic compression and decompression due to the compressibility of the material. Thus, a local acceleration consisting of Dirac δ functions is generated near the ablation front, where the oscillating acceleration exceeds the background acceleration driving the whole mass of the accelerated shell.

After the quasisteady ablative flow is established in the vicinity of the ablation front [see Fig. 1(c)], two typical laser intensity profiles of the specially modulated and unmodulated pulse shapes appear (see Fig. 2) and drive the accelerating target. As can be seen, a constant intensity of the unmodulated laser pulse as a reference case is always 3.0×10^{14} W/cm^2, which is consistent with the maximum value used in Fig. 1(b). According to the previous analysis, the ablative flow for the reference case continues to maintain its quasisteady system with the constant acceleration. To achieve sufficient stabilization, we assume that the specially modulated laser pulse consists of the perfectly symmetric square wave used in the simulations. Note that the dynamic stabilization of the modulated laser pulse depends strongly on the modulation amplitude and period of the symmetric square wave. Next, a general amplitude with 50% modulation depth is taken for the specially modulated laser pulse, which the peak and valley intensities are 4.5×10^{14} W/cm^2 and 1.5×10^{14} W/cm^2, respectively. Another stabilization factor is due to the modulation period of the symmetric square wave. Considering the stabilization effect and the difficulty of laser modulation, then the symmetric square wave with a period of 2.0 ns

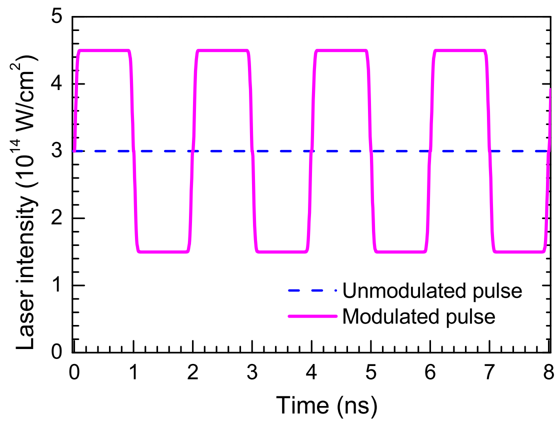

FIG. 2. Laser intensity profiles for unmodulated (dashed line) and for specially modulated (solid line) pulse shapes. A constant intensity of the unmodulated laser pulse as a reference case is always 3.0×10^{14} W/cm^2. The specially modulated case of 50% modulation depth consists of a symmetric square wave with a period of 2.0 ns, the peak intensity of 4.5×10^{14} W/cm^2, and the valley intensity of 1.5×10^{14} W/cm^2.

corresponding to the oscillation frequency is used in the following simulation, for which the rising and falling times of the modulated laser pulse are $\sim$100 ps. Theoretically, the considerable stabilization effect of the modulated laser improves if the period is sufficiently short. However, an optimal modulation period needs to be determined by considering the compressibility of the ablator materials and the response time of dense fluids, which is left to subsequent investigations. We limit the present study to the stability mechanism of the modulated laser pulse.

To further extend our understanding of the dynamically stabilized configuration, we compare the relevant laser-driven parameters of the unperturbed ablative flow driven by the specially modulated laser pulse with those of the unmodulated laser pulse, which reveals the inherent stability mechanism underlying the dynamically stabilized configuration. Figure 3 shows the temporal evolution of the relevant laser-driven parameters in two unperturbed ablative flows for modulated and unmodulated laser pulses, including the position s, acceleration g, pressure p_a of the ablation front, peak density, mass ablation rate $\dot{m}$, and ablation velocity V_a. For the reference case with the unmodulated laser pulse, Fig. 3 shows that the position of the ablation front follows a highly similar trajectory for modulated and unmodulated laser pulses. The acceleration profile for the unmodulated laser pulse at the ablation front remains unchanged, $g_{\text{unm}} \simeq 12.0$ μm/ns^2 during the quasisteady ablative flow, the pressure of the ablation front is constant at $p_a \simeq 39.0$ Mbar, and the peak density (ρ_h) gradually decreases over time due to the laser ablation. It is easy to find that the velocity of the ablation front in the unmodulated laser pulse continuous to increase linearly due to the constant acceleration. Moreover, the mass ablation rate ($\dot{m}$) at long times approaches a constant value of $\sim$ 0.98 g/(μs cm^2), and the ablation velocity ($V_a = \dot{m}/\rho_h$) remains approximately constant at $\sim$ 1.7 μm/ns and increases slightly with decreasing peak density ρ_h. In addition to this undistinguishable trajectory, the modulated laser pulse

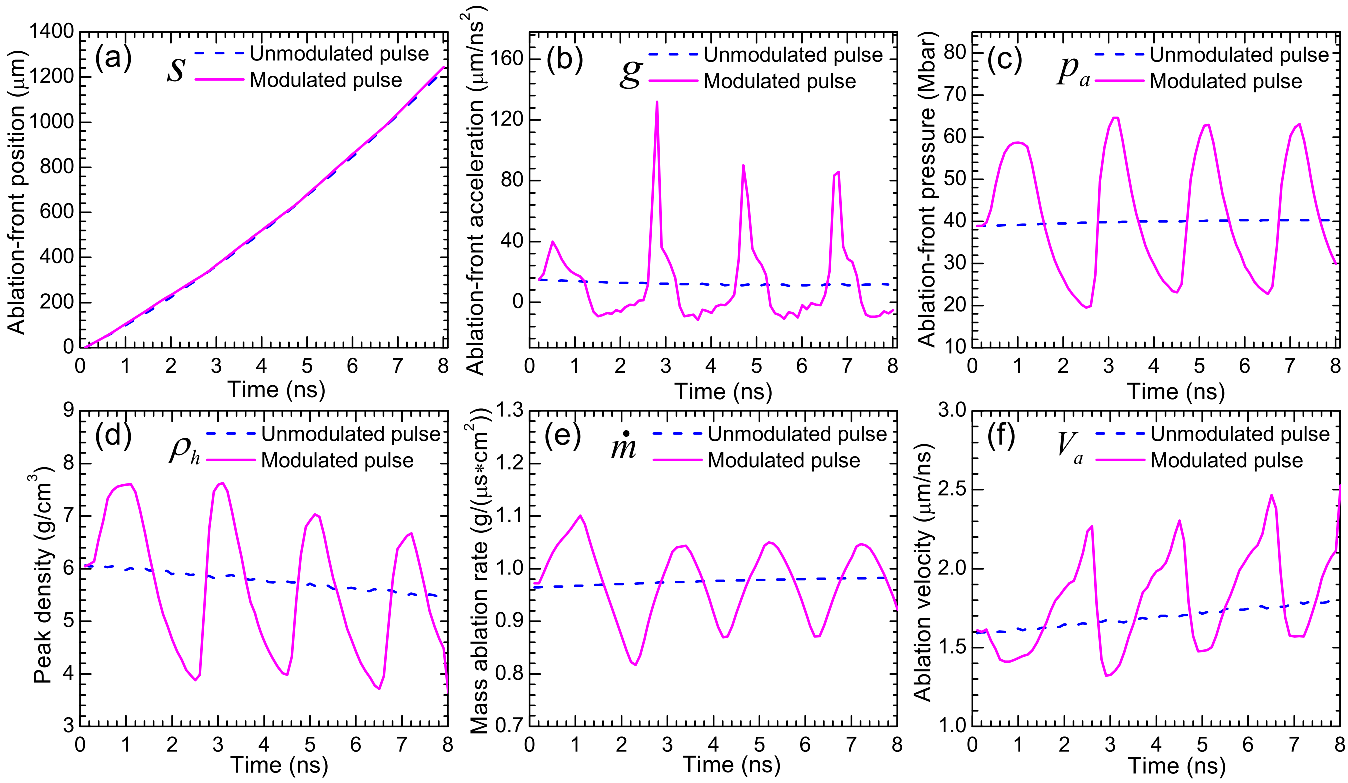

FIG. 3. Temporal evolution of the interesting laser-driven parameters in two unperturbed ablative flows for modulated (solid line) and unmodulated (dashed line) laser pulses. The laser parameters include (a) position s, (b) acceleration g, (c) pressure p_a of the ablation front (defined as the zone at half-peak density), (d) peak density ρ_h, (e) mass ablation rate $\dot{m}$, and (f) ablation velocity V_a.

produces a periodic oscillating system near the ablation front, which includes the oscillating distribution of the acceleration, ablation pressure, peak density, mass ablation rate, and ablation velocity, as shown in Figs. 3(b)–3(f). This result differs completely from that obtained in the reference case. Comparing the constant acceleration, the modulating acceleration $g_{\rm mod}$ with a sequence of positive Dirac δ functions and negative square waves is distributed in a complex and asymmetric manner. The dynamic stabilization of the RTI in the ablation front is supported theoretically by considering a modulation in the acceleration [38–40]. As in Fig. 3(c), the descent (ascent) of the oscillating ablation pressure corresponds to the phase of low-acceleration $g_{\rm mod} < g_{\rm unm}$ (high-acceleration $g_{\rm mod} > g_{\rm unm}$), which is a reciprocating motion with the compression and decompression process. Note that the velocity of the ablation front in the modulated laser case exhibits a periodic oscillation due to the oscillating distribution of the acceleration and ablation pressure, which is different from that of the unmodulated case. Although there is a periodic oscillation in the peak density, as shown in Fig. 3(d), the minimum oscillating peak density remains larger than that in the low-density ablated plasma, which weakly affects the perturbation growth at the ablation surface. For the laser-driven target, the mass ablation is an important factor in the perturbation evolution. Furthermore, comparing the distribution of the ablation velocity and acceleration, as shown in Figs. 3(b) and 3(f), the stabilization of the ablation velocity coincides with the acceleration in the ablative flow field driven by the specially modulated laser pulse. As previously described, the evolution of the perturbations at the ablation front is strongly affected by the presence of these oscillating results. These results suggest that the modulated laser pulse contributes considerably to the dynamic stabilization of the ARTI.

A series of shocks launched when the laser intensity is modulated causes the adiabat of the modulated laser pulse to likely differ from that of the unmodulated case, which affects the growth of the ARTI. Figure 4 compares the evolution of the adiabat near the ablation front for the modulated

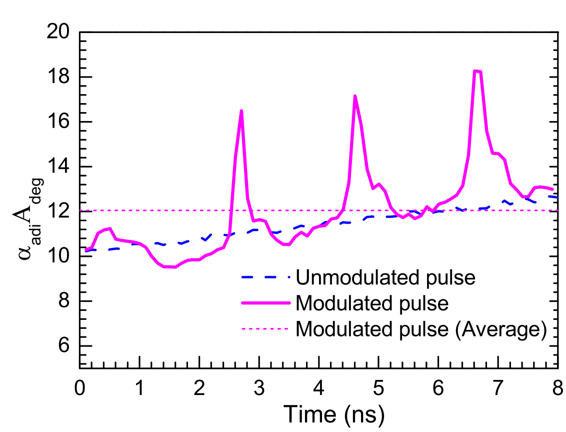

FIG. 4. Evolution of the adiabat near the ablation front for the modulated (solid line) laser pulse compared with that of the unmodulated (dashed line) laser pulse. The dotted line shows the average adiabat of the modulated laser pulse.

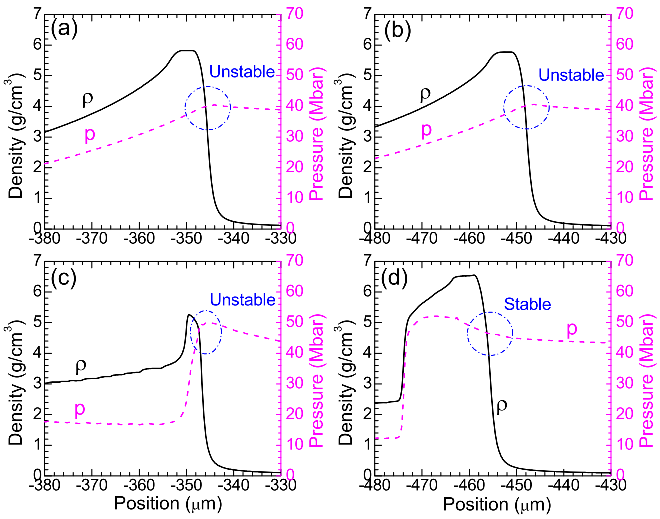

FIG. 5. Spatial profiles of density (solid lines) and pressure (dashed lines) near the ablation front for unmodulated (top row) and modulated (bottom row) laser pulses at 2.8 ns [(a) and (c)] and 3.5 ns [(b) and (d)]. The interface for the unmodulated laser pulse is always unstable because the pressure gradient opposes the density gradient. The interfaces for the modulated laser pulse at 2.8 ns and 3.5 ns are unstable and stable, respectively.

and unmodulated laser pulses. Here the adiabat is defined as $\alpha_{\mathrm{adi}} = P/P_{\mathrm{Fermi}}$, where $P = p_a$ is the ablation pressure and $P_{\mathrm{Fermi}} = \mathrm{A}_{\mathrm{deg}}\rho^{5/3}$ is the Fermi degenerate pressure with $\mathrm{A}_{\mathrm{deg}}$ being a constant for CH foil. The adiabat of the reference case increases slightly over time, and this small variation in α_{adi} can be neglected for the growth of the instability. For the dynamically stabilized configuration produced by the modulated laser pulse, the adiabat oscillates periodically, as shown in Fig. 4. A high adiabat reduces the growth of the ARTI [28]. Although the periodic oscillating adiabat produces an effective stabilization mechanism, the duration of the strong adiabat is relatively short compared with the reference case. Furthermore, the adiabat of the modulated laser pulse is averaged over the laser irradiation time, whose average value is only about 6.0% higher than that of the reference case, as shown in Fig. 4. In comparison with the reference case, the cumulative stabilizing effect of the strong adiabat in the modulated case decreases significantly, especially in the linear growth regime, which indicates a small difference between two typical laser intensity pulses. These results suggest that the stabilizing effect of the adiabat is not very important in the dynamically stabilized configuration.

We have presented the spatial variation of the ablative flow and a simple analysis of the periodic oscillating system to reveal the dynamically stabilized configuration. The spatial profiles of the density and pressure near the ablation front for unmodulated (top row) and modulated (bottom row) laser pulses at 2.8 and 3.5 ns are plotted in Figs. 5(a) and 5(c) and Figs. 5(b) and 5(d), respectively. Here two instantaneous ablation pressures of the modulated laser pulse at 2.8 and 3.5 ns are in the ascending and descending curves in Fig. 3(c), which corresponds to the peak and valley accelerations, respectively. For the quasisteady ablative flow generated by the unmodulated laser, Figs. 5(a) and 5(b) show that the ablation surface keeps unstable because the pressure gradient opposes the density gradient. Somewhat surprisingly, the simulation results show that the direction of the pressure gradient for the specially modulated laser pulse is reversed in Figs. 5(c) and 5(d), corresponding to the unstable and stable states, respectively. According to the distribution of the laser-driven parameters in the periodic oscillating system, we infer from the local potential field of the interface that the perturbation can be altered by the frequency and the periodic force due to the oscillation. In other words, the dynamic stabilization of the RTI in the ablation front can potentially reduce the perturbation growth compared with the reference case with the constant acceleration field.

B. Dynamic stabilization of single-mode ablative Rayleigh-Taylor instability

The stabilizing effect of laser-driven planar target irradiated by the modulated laser pulse is studied and analyzed through the single-mode perturbation at the ablation surface. The evolution of the ARTI with a sinusoidal small-amplitude perturbation for the modulated laser pulse is measured via numerical simulations. The growth of the ablation surface initiated by the same perturbation for the unmodulated laser pulse is considered as the reference case to understand the dynamic stabilization of the modulated laser pulse. Figure 6 illustrates the density contours of the single-mode ARTI initiated by a sinusoidal small-amplitude perturbation for unmodulated (top row) and modulated (bottom row) laser pulses at 2.0, 4.0, 6.0, and 8.0 ns, where the initial wavelength and its perturbation amplitude are $\lambda = 60$ μm and $A_0 \simeq 0.0034\lambda$, respectively. During the earlier stage of the instability [see Figs. 6(a1) and 6(b1)] a closely similar perturbation shape exists for the unmodulated and modulated laser pulses. However, as the perturbation grows, the perturbation amplitude of the modulated laser pulse becomes significantly smaller than that of the unmodulated laser pulse, especially at late time [see Figs. 6(a4) and 6(b4)]. The comparison of numerical results from the two cases indicates that the modulated laser pulse stabilizes the evolution of the ARTI. To more directly verify the dynamic stabilization of the modulated laser pulse, the single-mode perturbations with different wavelengths have been investigated. Figure 7 shows the evolution of the bubble-spike amplitudes of the single-mode ARTI initiated by the small-amplitude perturbation and irradiated by the unmodulated (dashed lines) and modulated (solid lines) laser pulses for wavelengths of 20, 60, and 90 μm. As seen in Fig. 7(a), the bubble-spike amplitude of the short-wavelength perturbation for the modulated laser pulse is almost zero about after 2.6 ns and noticeably smaller than for the unmodulated laser case, which indicates that the perturbation of this wavelength is completely suppressed. The stabilizing effect leads to the conclusion that the ablation surface with initial small-amplitude perturbations is stable for all wavelengths $\leqslant 20$ μm. As shown in Figs. 7(b) and 7(c), the bubble-spike amplitudes of the modulated laser remain less than those of the unmodulated case, but the stabilizing effect decreases with increasing perturbation wavelength. In addition, a periodic oscillation of the bubble-spike amplitude appears at the ablation surface for the

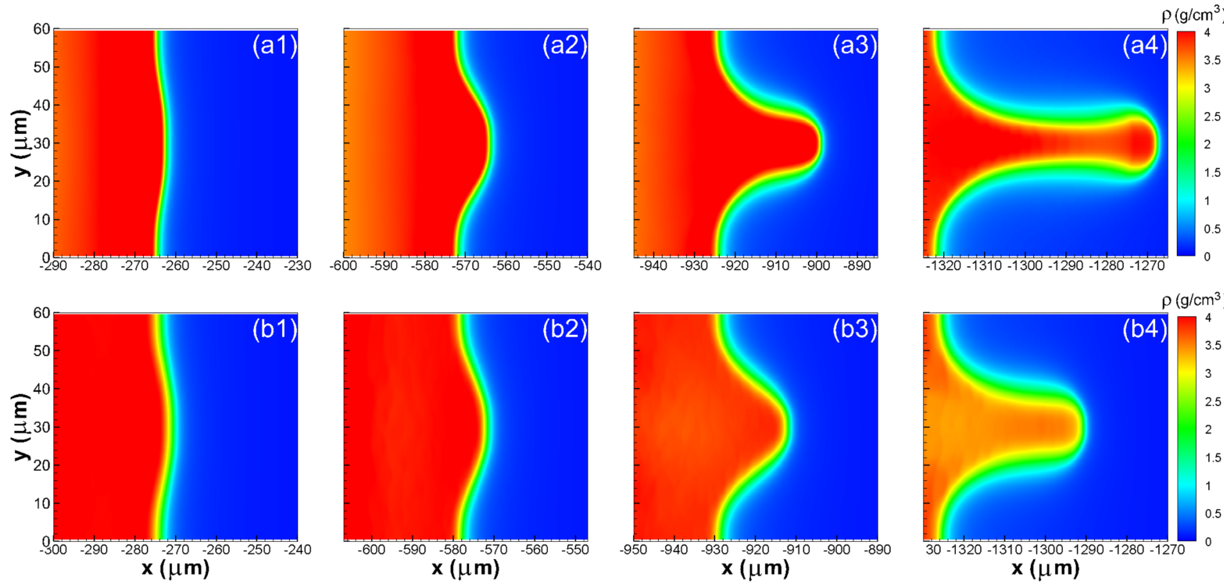

FIG. 6. Density contours of the single-mode ARTI initiated by a small-amplitude perturbation for unmodulated (top row) and modulated (bottom row) laser pulses at 2.0, 4.0, 6.0, and 8.0 ns. The initial wavelength and its perturbation amplitude are $\lambda = 60$ μm and $A_0 \simeq 0.0034\lambda$, respectively.

modulated laser pulse. This feature differs from the perturbation amplitude of the unmodulated laser pulse. A comparative analysis of different wavelength simulations shows that the stabilizing effect of the modulated laser on short-wavelength perturbations decreases significantly and gradually with increasing wavelength.

In addition to the dynamic stabilization, several physical effects cause the ablation front to become extremely complex. These physical effects include the oscillatory ablation pressure produced by the modulated laser pulse, mass ablation, and hydrodynamical instabilities. The following analysis concentrates on the evolution of amplitude of the ablation front over a single modulation period (i.e., the first modulation period). When the laser intensity increases, the driving acceleration of the dense compressed material under the greater ablation pressure is larger than that for the unmodulated case. Moreover, the peak density starts to grow sharply, as shown in Fig. 3(d), reducing the ablation velocity to less than that of the unmodulated case. Therefore, the amplitude of the ablation front grows and is suppressed by the combined effects of the large driving acceleration and the lower ablation velocity, as shown in Fig. 7 for the rising-amplitude stage. Correspondingly, when the laser intensity decreases, the perturbation amplitude is also affected by both the ablation pressure and mass ablation. As the ablation pressure decreases rapidly, the driving acceleration rapidly decreases and even reverses its direction, which in the case of the reversed driving acceleration causes the interface to oscillate in time. As the peak density rapidly decreases, the ablation velocity increases gradually beyond that of the unmodulated case, which produces greater ablative stabilization. Therefore, the reduction of the perturbation amplitude is mainly due to the large ablation velocity and

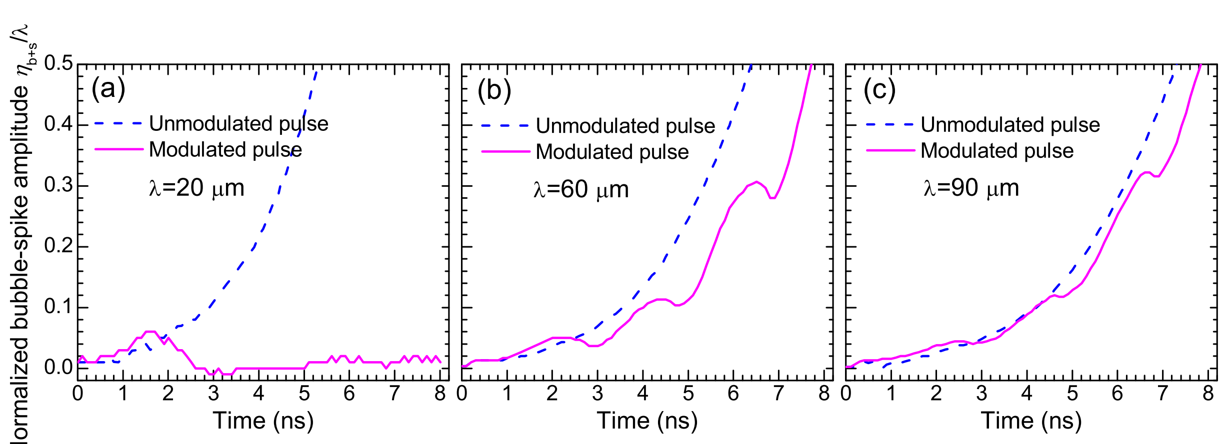

FIG. 7. Evolution of normalized bubble-spike amplitudes (η_{b+s}/λ) of the single-mode ARTI driven by the unmodulated (dashed lines) and modulated (solid lines) laser pulses for a perturbation with (a) $\lambda = 20$ μm, (b) 60 μm, and (c) 90 μm. The initial perturbation amplitudes for cases (a)–(c) are about 0.083, 0.206, and 0.323 μm, respectively.

the amplitude evolution becomes a stable ARTI oscillation under the influence of the reversed driving acceleration, as can be seen in Fig. 7 for the decreasing-amplitude stage. In fact, the ablation front in the modulated case undergoes ARTI growth, greater ablative stabilization, and stable ARTI oscillation for each modulation period.

Based on the previous analysis, the modulated laser plays a stabilizing role for the spatial evolution of the perturbed interface in the linear regime. Several theories [17,38–40] have been developed to explore the basic physical features of the linear growth in the ARTI. For instance, the modified Lindl formula [17] has been applied to the steady ablation front with the unmodulated laser pulse, the Betti stability theory [38] has been applied to the unsteady ablation front with the temporally modulated laser pulse, and the Piriz model [39,40] has been applied to the dynamic stabilization of the ablation front with the asymmetric modulation of the driving acceleration.

To capture the basic physical features of the dynamic stabilization of the modulated laser pulse, the stability analysis of the present work focuses on the driving acceleration of the ablation front. Figure 8(a) shows the temporal evolution of the driving accelerations obtained from the unmodulated and modulated laser pulses. The driving acceleration (dashed line) of the ablation front directly driven by the unmodulated laser pulse approaches a constant $g_{\mathrm{unm}} \simeq 12.0$ μm/ns^2. The modulating acceleration (solid line) of the ablation front is generated by the modulated laser pulse, with a period of 2.0 ns. The distribution of the modulating acceleration is complex and asymmetric and consists of positive Dirac δ functions and negative square driving waves. Moreover, the proportion of the square driving wave is more prominent. To better understand the stabilization of the modulating acceleration, we introduce the oscillatory acceleration (dotted line) with an asymmetric square wave at the ablation front. This instantaneous modulating acceleration is then approximated by $g(t) = g_0 + b\Gamma(\omega t)$, where $g_0 \simeq 12.2$ μm/ns^2 is the background acceleration, and $b\Gamma(\omega t)$ is the asymmetric square-wave modulation of the oscillatory acceleration (see Fig. 1 in Ref. [40]). Here the minimum and maximum of the instantaneous modulating acceleration are $g_{\min} \simeq -3.9$ μm/ns^2 with a duration of $t_{\min} \sim 1.52$ ns and $g_{\max} \simeq 63.3$ μm/ns^2 with a duration of $t_{\max} \sim 0.48$ ns, respectively, with the condition $(g_{\max} - g_0)t_{\max} = (g_0 - g_{\min})t_{\min}$ imposed to ensure that the average acceleration of the ablation front is $\langle g(t)\rangle \simeq g_0$. In addition, other associated parameters are the ablation velocity of the ablation front $\langle V_a\rangle = 1.7$ μm/ns and the characteristic scale length $\langle L_m\rangle = 0.6$ μm, where the angle brackets $\langle\rangle$ represent the average from 2.0 to 6.0 ns in the linear growth phase.

Growth and oscillation of the perturbation amplitude are observed in many simulations with the modulated laser pulse, leading to the conclusion that the analytical description of these simulations depends strongly on the instability growth rate γ and the oscillation frequency ω. Each simulation result in the linear regime is taken into consideration, where the perturbation amplitude includes the growth component varying as an exponential waveform and the oscillation component varying as a sinusoidal waveform. In our analytical procedure, the perturbation amplitude is then well fitted by $\eta_0 \exp(\gamma t)[1 + a_0 \cos(\omega t + \theta_0)]$, which produces a linear growth rate, where η_0 is the initial perturbation amplitude, a_0 is an oscillation parameter, and θ_0 is the initial phase.

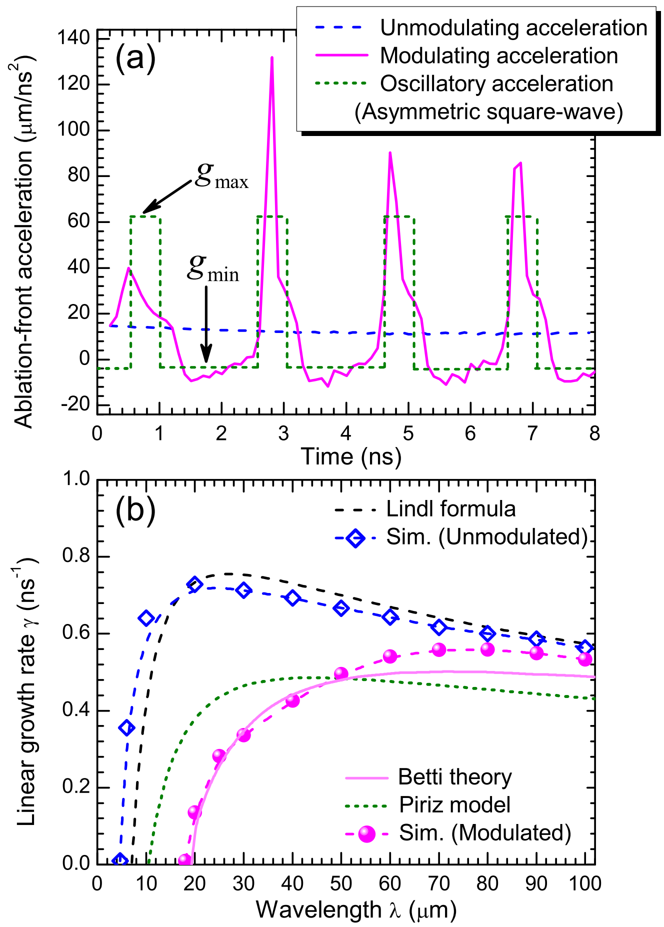

FIG. 8. (a) Temporal evolution of driving accelerations obtained from unmodulated (dashed line) and modulated (solid line) laser pulses. The dotted line represents an asymmetric square-wave modulation of the oscillatory acceleration. (b) Linear growth rates obtained from numerical simulations with unmodulated (diamonds) and modulated (spheres) laser pulses, Lindl formula (dashed line) [17], Betti theory [38], and the Piriz model (dashed line) [39,40]. The cutoff wavelengths of the numerical simulations for the unmodulated and modulated laser pulses are about 5.0 and 20.0 μm, respectively.

Figure 8(b) compares the linear growth rates obtained from numerical simulations with the unmodulated and modulated laser pulses, the Lindl formula [17], Betti theory [38], and the Piriz model [39,40]. For the unmodulated laser pulse, the linear growth rates obtained by fitting the simulations are reasonably consistent with that obtained using the Lindl formula, $\gamma = \alpha\sqrt{kg/(1 + kL_m)} - \beta kV_a$, where the fitting coefficients $\alpha = 0.90$ and $\beta = 1.65$, and the acceleration $g = g_{\mathrm{unm}} \simeq 12.0$ μm/ns^2, and the characteristic scale length $L_m \simeq 0.6$ μm. The simulation results indicate that the numerical code for the laser-driven planar plastic target is reliable and accurate.

For the modulated laser pulse, the dynamic stabilization of the ablation front for the oscillatory acceleration is validated by Betti [38], Piriz [39,40], and the above observation. The simulation results for the modulated laser are consistent with the theoretical estimations. The numerical solution of the

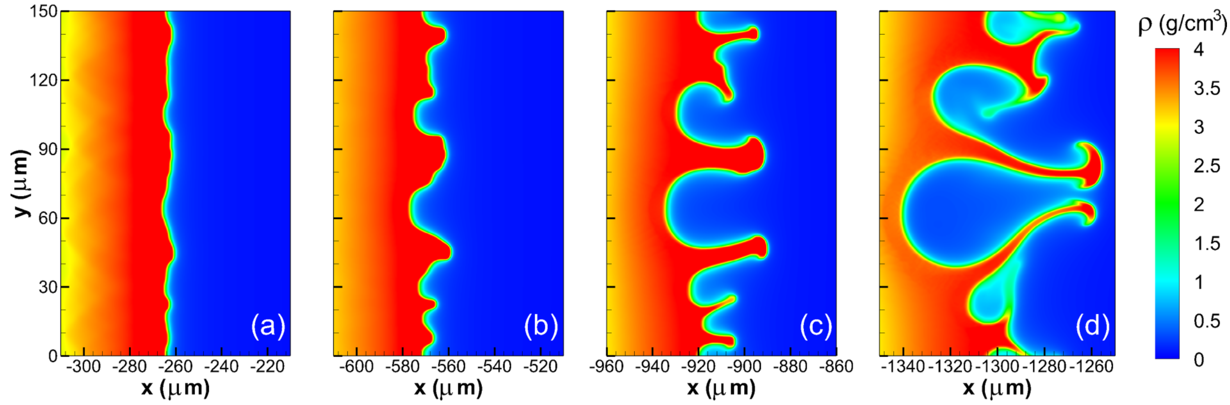

FIG. 9. Density contours of initial multimode ARTI for unmodulated laser pulse at times (a) 2.0 ns, (b) 4.0 ns, (c) 6.0 ns, and (d) 8.0 ns. The maximum initial wavelength and its perturbation amplitude are $\lambda_3 = 50$ μm and $A_{3,0} \simeq 0.552$ μm.

instability growth rate is obtained by replacing the sinusoidal form in the Mathieu equation of Ref. [38] with the instantaneous modulating acceleration, and the analytical solution of the linear growth rates is calculated by applying the Piriz model to the oscillatory acceleration with the asymmetric square-wave modulation [40]. Overall, the linear growth rates obtained from the modulated laser are significantly smaller than that of the unmodulated case. In particular, the cutoff wavelengths of the numerical simulations for the unmodulated and modulated laser pulses are about 5.0 and 20.0 μm, respectively. The small-amplitude perturbations up to the cutoff wavelength are completely inhibited by the modulated laser. These results show that the ablation front driven by the modulated laser has been dynamically stabilized for the reduction of the growth rate and the enhancement of the cutoff wavelength. In general, the laser modulation provides the dynamically stabilized configuration near the ablation surface and can be an efficient method for mitigating perturbations.

C. Dynamic stabilization of multimode ablative Rayleigh-Taylor instability

In this section we address how the stabilization effect of the modulated laser pulse affects multimode perturbations. It is clear that the hydrodynamic instability involving multimode perturbations is seeded by surface roughness and drive asymmetries. These multimode perturbations, consisting of random amplitudes and phases, grow into the nonlinear regime and lead to a wider mixing region. The nonlinear evolution of initial multimode perturbations in the presence of the unmodulated laser pulse is used as a reference case is easily to understand because the detailed features of the stabilization effect of the modulated laser pulse are easy yo understand. Figure 2 shows these two typical laser pulse shapes. The multimode perturbations with small amplitudes $A_{m,0} = A_0/k_m^{\theta}$, a continuous spectrum $m \geqslant m_{\min}$, and random phases $\phi_{m,0}$ are expressed as $\sum_{m_{\min}} A_{m,0} \cos(k_m y + \phi_{m,0}) \exp(-k_m|x - x_0|)$, where A_0 is a small parameter, $k_m = 2\pi/\lambda_m$ is the wave number, $\lambda_m = L_y/m$ is the wavelength of the perturbation mode m, L_y is the length of the simulation domain in the transverse direction, $\theta = 1.6$ is a fixed spectrum index, $m_{\min}$ is the minimum perturbation mode, and x_0 is the location of the ablation front. The minimum perturbation mode $m_{\min}$ for multimode perturbations corresponds to the maximum wavelength. Figure 9 illustrates the density contours of initial small-amplitude perturbations for the unmodulated laser pulse at times $t = 2.0$, 4.0, 6.0, and 8.0 ns, where the maximum wavelength and its initial amplitude are $\lambda_3 = 50$ μm and $A_{3,0} \simeq 0.011\lambda_3$, respectively. As shown in Figs. 9(a) and 9(b), the amplitude and the spatial scale of the ablation surface are relatively small at the earlier stage of the perturbation growth, when the perturbation amplitude of each mode grows exponentially in time. After the exponential growth, the structure of bubbles and spikes becomes larger in the nonlinear regime [see Fig. 9(c)], where the perturbation amplitude of the dominant modes is comparable to its wavelength. Due to the bubble competition, as shown in Fig. 9(d), the larger bubbles become broader and the smaller bubbles are gradually absorbed by the nearby larger bubbles, with the number of dominant bubbles gradually decreasing and their wavelength increasing. The bubble-front evolution obtained from the current simulation is consistent with the results of Oron *et al.* [59]. The small-amplitude perturbations at the ablation surface evolve into a large and complicated structure over time, and the large-scale structure gradually assumes a leading role. In parallel, the width of the mixing region increases, with the dominant bubbles becoming broader and the spikes narrower.

To capture how the modulated laser pulse stabilizes the nonlinear evolution of the system, Fig. 10 shows a typical example of the density contours of an initial multimode ARTI for the modulated laser pulse at times $t = 2.0$, 4.0, 6.0, and 8.0 ns. The maximum initial wavelength and its perturbation amplitude are the same as in Fig. 9 to facilitate comparison with that the unmodulated case. Figure 10 shows that the evolutionary system of the ablation surface for the modulated laser described here differs clearly from the reference case. The most interesting difference occurs in the spatial structure and the mixing layer. Compared with the unmodulated case, the simulation results show that the small-scale structures have been suppressed, leading to a very smooth surface. This is due to the fact that the modulated laser plays a stronger stabilizing role than the unmodulated laser, as discussed previously and shown in Fig. 8(b): more short wavelengths (up to the cutoff wavelength) in the dynamically stabilized configuration are completely inhibited. In the later phase, the mixing layer of the ablative surface is thinner than in the unmodulated

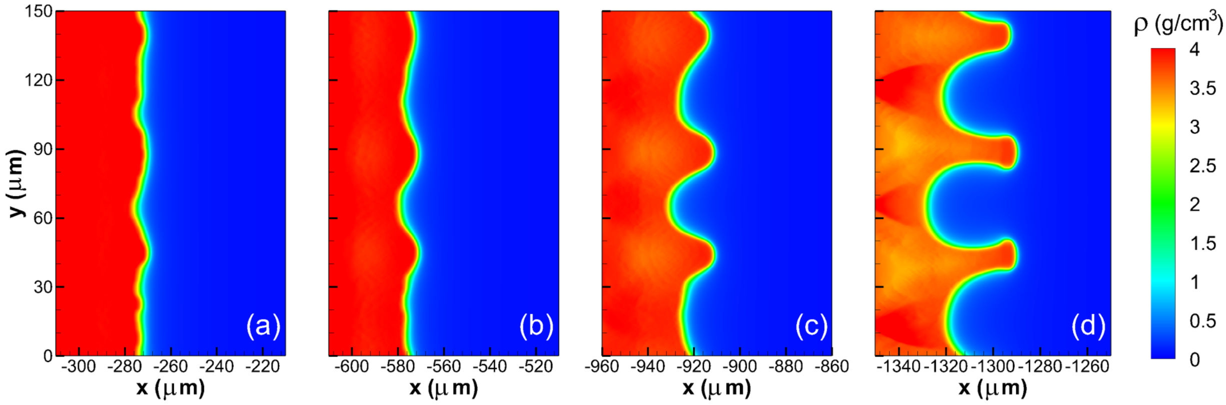

FIG. 10. Density contours of initial multimode ARTI for modulated laser pulse at times (a) 2.0 ns, (b) 4.0 ns, (c) 6.0 ns, and (d) 8.0 ns. The maximum initial wavelength and its perturbation amplitude are the same as in Fig. 9.

case, which indicates that the modulated laser stabilizes the growth of the mixing region. Furthermore, the simulation of the modulated laser pulse is similar to the unmodulated case. In both cases the size of the dominant bubble gradually increases and the number of bubbles decreases. Figures 9 and 10 show that the modulated laser stabilizes the ablation surface and inhibits instability growth. Considering how the modulated laser stabilizes multimode perturbations is thus the next step.

To investigate in detailed the stabilizing effect of the modulated laser pulse, the spatial structure of the ablation surface is subjected to a Fourier analysis. At the late stage of the development, the structure is large and complicated, as shown in Fig. 9(d), so a Fourier analysis may be inaccurate. Figure 11 compares the Fourier amplitude distributions as a function of mode number at 2.0, 4.0, and 6.0 ns, converted into areal density and irradiated by unmodulated and modulated laser pulses. During the earlier stage of multimode perturbations [see Fig. 11(a)], there is a closely similar Fourier amplitude distribution for these two cases due to a weaker stabilization of the modulated laser pulse on the ablation surface. Due to growing perturbations, as shown in Fig. 11(b), the high-mode amplitudes of the modulated laser case are significantly smaller than those of the unmodulated laser, which indicates that the modulated laser more strongly stabilize the high-mode perturbations than the low-mode perturbations. In the subsequent phase of the perturbation growth, the low-mode components corresponding to the long-wavelength perturbations are also gradually stabilized by the modulated laser, as shown in Fig. 11(c). The Fourier analysis shows that the short-wavelength perturbations are more stabilized by the modulated laser than the long-wavelength perturbations.

The stabilization effect of the modulated laser pulse contributes to reducing the width of the mixing layer, a remarkable feature which becomes evident upon comparing the unmodulated and modulated laser pulses in Figs. 9 and 10. The modulated laser stabilizes multimode perturbations at the ablation surface, the width of the mixing layer is reduced, and long-wavelength perturbations are the main component of the spatial structure. These main components make a dominant contribution to the growth of the nonlinear mixing region. The other simulation domains ($L_y = 240$ and 360 μm) corresponding to the maximum initial wavelengths of 80 and 120 μm are considered now to estimate how the modulated laser pulse stabilizes the growth of the nonlinear mixing region.

Figure 12 plots the evolution of the widths of the mixing layers for the unmodulated and modulated laser pulses for simulation domains $L_y = 150$, 240, and 360 μm in the y direction. The maximum initial wavelengths (i.e., the perturbation amplitudes) for the three simulation domains are 50 μm ($\sim$0.552 μm), 80 μm ($\sim$0.858 μm), and 120 μm ($\sim$1.143 μm), respectively. As seen in Fig. 12, the widths of the mixing layer for the modulated laser are significantly less than those for the unmodulated laser, and they oscillate

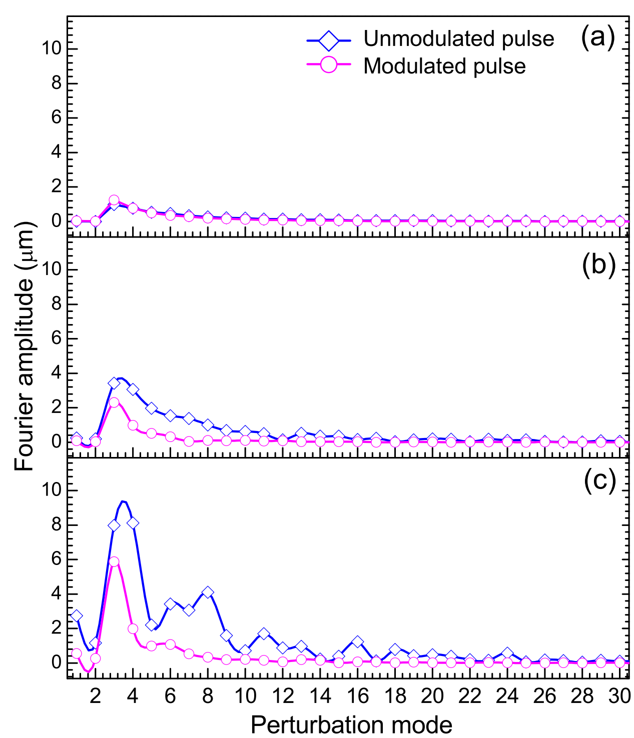

FIG. 11. Comparison of Fourier amplitude distributions as a function of mode number at (a) 2.0 ns, (b) 4.0 ns, and (c) 6.0 ns, converted in the areal density and irradiated by unmodulated laser pulses (diamonds) and modulated laser pulses (spheres).

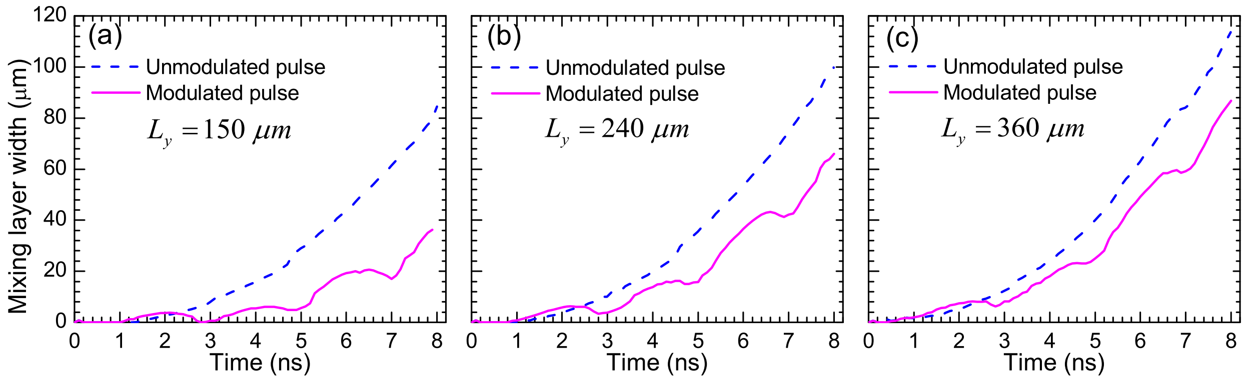

FIG. 12. Evolution of mixing layer widths for unmodulated (dashed lines) and modulated (solid lines) laser pulses for simulation domains (a) $L_y = 150$ μm, (b) $L_y = 240$ μm, and (c) $L_y = 360$ μm in the y direction. The maximum initial wavelengths (i.e., the perturbation amplitudes) for three cases (a)–(c) are 50 μm (~ 0.552 μm), 80 μm (~ 0.858 μm) and 120 μm (~ 1.143 μm), respectively. The one-dimensional parameters of the unmodulated and modulated pulses are the same as in Figs. 9 and 10.

periodically, which indicates that the dynamic stabilization is generated by considering the modulated laser pulse. Figure 12 shows that the stabilization effect of the modulated laser pulse decreases as the maximum wavelength increases.

IV. CONCLUSIONS

This work numerically studies the dynamic stabilization of the ARTI in the presence of a temporally modulated laser pulse, which is a prominent feature in comparison with the reference case of the unmodulated laser pulse. We analyze the physical features of the relevant laser-driven parameters in the unperturbed ablative flows. The results show that the modulated laser pulse produces a periodic oscillating system near the ablation front, including the acceleration, pressure, peak density, mass ablation rate, ablation velocity, and adiabat, which is completely different from the situation in the reference case. Moreover, analyzing the spatial profiles of the density and pressure near the ablation front for the modulated and unmodulated laser pulses reveals the inherent physical mechanism underlying the dynamically stabilized configuration.

Subsequently, we compare the interfacial evolution of the single-mode ARTI for the modulated laser pulse with that of the unmodulated case. The results show that the modulated laser stabilizes the growth of the ARTI. A comparison of the linear growth rates obtained by fitting the simulated data indicates that the linear growth rates obtained from the modulated laser are smaller than those obtained in the unmodulated case. In particular, the cutoff wavelength for the modulated laser pulse is about 20 μm, which is significantly greater than the unmodulated case (5 μm). Moreover, the measured growth rates at the ablation front for the modulated laser are generally consistent with previous theoretical estimates obtained by substituting the modulating acceleration into Betti stability theory [38], and by applying the Piriz model [39,40] with the asymmetric square-wave modulation acceleration.

As in the multimode ARTI, we report several features of the ablation surface in the presence of the specially modulated laser pulse. The stabilization effect of the modulated laser contributes to suppressing the small-scale structures and reduces the width of the mixing layer. Applying the method of Fourier analysis shows that the short-wavelength perturbations are more stabilized by the modulated laser for long wavelengths. The present work shows that the dynamic stabilization effect of the modulated laser pulse decreases as the maximum wavelength increases.

Finally, we conclude that the temporally modulated laser pulse produces the dynamically stabilized configuration and contributes to reducing the growth of the ARTI and of the mixing-layer width. Therefore, a periodically modulated laser pulse is an efficient method for mitigating perturbations, and should be the subject of experimentation on a practical laser facility to develop applications involving the design of direct-drive ICF ignition targets.

ACKNOWLEDGMENTS

The authors are very grateful to J. W. Li at the Institute of Applied Physics and Computational Mathematics, and Y. X. Liu at the China University of Mining and Technology for useful discussions on the code and postprocessing. This work was supported by the National Key R&D Program of China (Grant No. 2023YFA1608400), the National Natural Science Foundation of China (Grants No. 12005008, No. 12005022, No. 11975053, No. 12105022, No. 12375237, No. 12235041, and No. 11675026), and the Natural Science Foundation of Top Talent of SZTU (Grant No. GDRC202209).

[1] J. Nuckolls, L. Wood, A. Thiessen, and G. Zimmerman, Laser compression of matter to super-high densities: Thermonuclear (CTR) applications, Nature (London) **239**, 139 (1972).

[2] S. Atzeni and J. Meyer-ter-Vehn, *The Physics of Inertial Fusion: Beam Plasma Interaction Hydrodynamics, Hot Dense Matter* (Oxford University Press, Oxford, 2004).

[3] X. T. He, J. W. Li, Z. F. Fan, L. F. Wang, J. Liu, K. Lan, J. F. Wu, and W. H. Ye, A hybrid-drive nonisobaric-ignition scheme for inertial confinement fusion, Phys. Plasmas **23**, 082706 (2016).

[4] A. L. Kritcher, C. V. Young, H. F. Robey, C. R. Weber, A. B. Zylstra, O. A. Hurricane, D. A. Callahan, J. E. Ralph, J. S. Ross, K. L. Baker *et al.*, Design of inertial fusion implosions reaching the burning plasma regime, Nat. Phys. **18**, 251 (2022).

[5] H. Abu-Shawareb, R. Acree, P. Adams, J. Adams, B. Addis, R. Aden, P. Adrian, B. B. Afeyan, M. Aggleton, L. Aghaian *et al.*, Lawson criterion for ignition exceeded in an inertial fusion experiment, Phys. Rev. Lett. **129**, 075001 (2022).

[6] X. T. He and W. Y. Zhang, Inertial fusion research in China, Eur. Phys. J. D **44**, 227 (2007).

[7] R. Betti and O. A. Hurricane, Inertial-confinement fusion with lasers, Nat. Phys. **12**, 435 (2016).

[8] L. Rayleigh, Investigation of the character of the equilibrium of an incompressible heavy fluid of variable density, Proc. London Math. Soc. **s1-14**, 170 (1882).

[9] G. Taylor, The instability of liquid surfaces when accelerated in a direction perpendicular to their planes, Proc. R. Soc. London, Ser. A **201**, 192 (1950).

[10] O. A. Hurricane, D. A. Callahan, D. T. Casey, P. M. Celliers, C. Cerjan, E. L. Dewald, T. R. Dittrich, T. Döppner, D. E. Hinkel, L. F. B. Hopkins *et al.*, Fuel gain exceeding unity in an inertially confined fusion implosion, Nature (London) **506**, 343 (2014).

[11] L. F. Wang, W. H. Ye, X. T. He, J. F. Wu, Z. F. Fan, C. Xue, H. Y. Guo, W. Y. Miao, Y. T. Yuan, J. Q. Dong *et al.*, Theoretical and simulation research of hydrodynamic instabilities in inertial-confinement fusion implosions, Sci. China: Phys., Mech. Astron. **60**, 055201 (2017).

[12] Y. Zhou, T. T. Clark, D. S. Clark, S. G. Glendinning, M. A. Skinner, C. M. Huntington, O. A. Hurricane, A. M. Dimits, and B. A. Remington, Turbulent mixing and transition criteria of flows induced by hydrodynamic instabilities, Phys. Plasmas **26**, 080901 (2019).

[13] S. W. Haan, J. D. Lindl, D. A. Callahan, D. S. Clark, J. D. Salmonson, B. A. Hammel, L. J. Atherton, R. C. Cook, M. J. Edwards, S. Glenzer *et al.*, Point design targets, specifications, and requirements for the 2010 ignition campaign on the National Ignition Facility, Phys. Plasmas **18**, 051001 (2011).

[14] S. Bodner, Rayleigh-Taylor instability and laser-pellet fusion, Phys. Rev. Lett. **33**, 761 (1974).

[15] H. Takabe, K. Mima, L. Montierth, and R. L. Morse, Self-consistent growth rate of the Rayleigh-Taylor instability in an ablatively accelerating plasma, Phys. Fluids **28**, 3676 (1985).

[16] J. Sanz, Self-consistent analytical model of the Rayleigh-Taylor instability in inertial confinement fusion, Phys. Rev. Lett. **73**, 2700 (1994).

[17] J. Lindl, Development of the indirect-drive approach to inertial confinement fusion and the target physics basis for ignition and gain, Phys. Plasmas **2**, 3933 (1995).

[18] V. N. Goncharov, R. Betti, R. L. McCrory, P. Sorotokin, and C. P. Verdon, Self-consistent stability analysis of ablation fronts with large Froude numbers, Phys. Plasmas **3**, 1402 (1996).

[19] R. Betti, V. N. Goncharov, R. L. McCrory, P. Sorotokin, and C. P. Verdon, Self-consistent stability analysis of ablation fronts in inertial confinement fusion, Phys. Plasmas **3**, 2122 (1996).

[20] L. F. Wang, W. H. Ye, Z. M. Sheng, W.-S. Don, Y. J. Li, and X. T. He, Preheating ablation effects on the Rayleigh-Taylor instability in the weakly nonlinear regime, Phys. Plasmas **17**, 122706 (2010).

[21] K. Lan, J. Liu, Z. Li, X. Xie, W. Huo, Y. Chen, G. Ren, C. Zheng, D. Yang, S. Li *et al.*, Progress in octahedral spherical hohlraum study, Matter Radiat. Extremes **1**, 8 (2016).

[22] K. Shigemori, H. Azechi, M. Nakai, M. Honda, K. Meguro, N. Miyanaga, H. Takabe, and K. Mima, Measurements of Rayleigh-Taylor growth rate of planar targets irradiated directly by partially coherent light, Phys. Rev. Lett. **78**, 250 (1997).

[23] S. Fujioka, First observation of density profile in directly laser-driven polystyrene targets for ablative Rayleigh-Taylor instability research, Phys. Plasmas **10**, 4784 (2003).

[24] L. F. Wang, W. H. Ye, and X. T. He, Density gradient effects in weakly nonlinear ablative Rayleigh-Taylor instability, Phys. Plasmas **19**, 012706 (2012).

[25] R. Betti, V. N. Goncharov, R. L. McCrory, and C. P. Verdon, Growth rates of the ablative Rayleigh-Taylor instability in inertial confinement fusion, Phys. Plasmas **5**, 1446 (1998).

[26] W. H. Ye, W. Y. Zhang, and X. T. He, Stabilization of ablative Rayleigh-Taylor instability due to change of the Atwood number, Phys. Rev. E **65**, 057401 (2002).

[27] S. E. Bodner, D. G. Colombant, J. H. Gardner, R. H. Lehmberg, S. P. Obenschain, L. Phillips, A. J. Schmitt, J. D. Sethian, R. L. McCrory, W. Seka *et al.*, Direct-drive laser fusion: Status and prospects, Phys. Plasmas **5**, 1901 (1998).

[28] V. A. Smalyuk, V. N. Goncharov, K. S. Anderson, R. Betti, R. S. Craxton, J. A. Delettrez, D. D. Meyerhofer, S. P. Regan, and T. C. Sangster, Measurements of the effects of the intensity pickets on laser imprinting for direct-drive, adiabat-shaping designs on OMEGA, Phys. Plasmas **14**, 032702 (2007).

[29] L. F. Wang, W. H. Ye, J. F. Wu, J. Liu, W. Y. Zhang, and X. T. He, Main drive optimization of a high-foot pulse shape in inertial confinement fusion implosions, Phys. Plasmas **23**, 122702 (2016).

[30] J. Li, R. Yan, B. Zhao, J. Zheng, H. Zhang, and X. Lu, Mitigation of the ablative Rayleigh-Taylor instability by nonlocal electron heat transport, Matter Radiat. Extremes **7**, 055902 (2022).

[31] S. Fujioka, A. Sunahara, K. Nishihara, N. Ohnishi, T. Johzaki, H. Shiraga, K. Shigemori, M. Nakai, T. Ikegawa, M. Murakami *et al.*, Suppression of the Rayleigh-Taylor instability due to self-radiation in a multiablation target, Phys. Rev. Lett. **92**, 195001 (2004).

[32] S. X. Hu, G. Fiksel, V. N. Goncharov, S. Skupsky, D. D. Meyerhofer, and V. A. Smalyuk, Mitigating laser imprint in direct-drive inertial confinement fusion implosions with high-Z dopants, Phys. Rev. Lett. **108**, 195003 (2012).

[33] B. L. Yang, L. F. Wang, W. H. Ye, and C. Xue, Magnetic field gradient effects on Rayleigh-Taylor instability with continuous magnetic field and density profiles, Phys. Plasmas **18**, 072111 (2011).

[34] M. J.-E. Manuel, B. Khiar, G. Rigon, B. Albertazzi, S. R. Klein, F. Kroll, F.-E. Brack, T. Michel, P. Mabey, S. Pikuz *et al.*, On the study of hydrodynamic instabilities in the presence of background magnetic fields in high-energy-density plasmas, Matter Radiat. Extremes **6**, 026904 (2021).

[35] W. H. Ye, L. F. Wang, and X. T. He, Spike deceleration and bubble acceleration in the ablative Rayleigh-Taylor instbaility, Phys. Plasmas **17**, 122704 (2010).

[36] L. F. Wang, W. H. Ye, X. T. He, W. Y. Zhang, Z. M. Sheng, and M. Y. Yu, Formation of jet-like spikes from the ablative Rayleigh-Taylor instability, Phys. Plasmas **19**, 100701 (2012).

[37] J. P. Boris, Comments Plasma Phys. Controlled Fusion **3**, 1 (1977).

[38] R. Betti, R. L. McCrory, and C. P. Verdon, Stability analysis of unsteady ablation fronts, Phys. Rev. Lett. **71**, 3131 (1993).

[39] A. R. Piriz, L. Di Lucchio, and G. Rodriguez Prieto, Dynamic stabilization of Rayleigh-Taylor instability in an ablation front, Phys. Plasmas **18**, 012702 (2011).

[40] A. R. Piriz, L. Di Lucchio, G. Rodriguez Prieto, and N. A. Tahir, Vibration waveform effects on dynamic stabilization of ablative Rayleigh-Taylor instability, Phys. Plasmas **18**, 082705 (2011).

[41] S. A. Piriz, A. R. Piriz, and N. A. Tahir, Rayleigh-Taylor instability in ion beam driven ablation fronts, Phys. Plasmas **16**, 082706 (2009).

[42] G. Wolf, Dynamic stabilization of the interchange instability of a liquid-gas interface, Phys. Rev. Lett. **24**, 444 (1970).

[43] G. Rodriguez Prieto, A. R. Piriz, J. J. Lopez Cela, and N. A. Tahir, Dynamic stabilization of Rayleigh-Taylor instability: Experiments with Newtonian fluids as surrogates for ablation fronts, Phys. Plasmas **20**, 012706 (2013).

[44] F. Troyon and R. Gruber, Theory of the dynamic stabilization of the Rayleigh-Taylor instability, Phys. Fluids **14**, 2069 (1971).

[45] A. R. Piriz, G. R. Prieto, I. M. Díaz, J. J. López Cela, and N. A. Tahir, Dynamic stabilization of Rayleigh-Taylor instability in Newtonian fluids, Phys. Rev. E **82**, 026317 (2010).

[46] A. R. Piriz, S. A. Piriz, and N. A. Tahir, Dynamic stabilization of classical Rayleigh-Taylor instability, Phys. Plasmas **18**, 092705 (2011).

[47] G. Dimonte and M. Schneider, Turbulent Rayleigh-Taylor instability experiments with variable acceleration, Phys. Rev. E **54**, 3740 (1996).

[48] G. Boffetta, M. Magnani, and S. Musacchio, Suppression of Rayleigh-Taylor turbulence by time-periodic acceleration, Phys. Rev. E **99**, 033110 (2019).

[49] P. K. Kaw and J. M. Dawson, Laser-induced anomalous heating of a plasma, Phys. Fluids **12**, 2586 (1969).

[50] M. H. Emery, J. H. Orens, J. H. Gardner, and J. P. Boris, Influence of nonuniform laser intensities on ablatively accelerated targets, Phys. Rev. Lett. **48**, 253 (1982).

[51] J. P. Dahlburg, J. H. Gardner, M. H. Emery, and J. P. Boris, Hydrodynamic evolution of the split-foil laser target, Phys. Rev. A **35**, 2737 (1987).

[52] L. Spitzer and R. Härm, Transport phenomena in a completely ionized gas, Phys. Rev. **89**, 977 (1953).

[53] Z. Li, L. Wang, J. Wu, and W. Ye, Numerical study on the laser ablative Rayleigh-Taylor instability, Acta Mech. Sin. **36**, 789-796 (2020).

[54] B. Einfeldt, C. D. Munz, P. L. Roe, and B. Sjögreen, On Godunov-type methods for gas dynamics, J. Comput. Phys. **92**, 273 (1991).

[55] R. D. Falgout, J. E. Jones, and U. M. Yang, *Solution of Partial Differential Equations on Parallel Computers* (Springer, Berlin, 2006).

[56] R. J. Taylor, A. L. Velikovich, J. P. Dahlburg, and J. H. Gardner, Saturation of laser imprint on ablatively driven plastic targets, Phys. Rev. Lett. **79**, 1861 (1997).

[57] J. W. Bates, A. J. Schmitt, M. Karasik, and S. T. Zalesak, Numerical simulations of the ablative Rayleigh-Taylor instability in planar inertial-confinement-fusion targets using the FastRad3D code, Phys. Plasmas **23**, 122701 (2016).

[58] J. H. Gardner, S. E. Bodner, and J. P. Dahlburg, Numerical simulation of ablative Rayleigh-Taylor instability, Phys. Fluids B **3**, 1070 (1991).

[59] D. Oron, U. Alon, and D. Shvarts, Scaling laws of the Rayleigh-Taylor ablation front mixing zone evolution in inertial confinement fusion, Phys. Plasmas **5**, 1467 (1998).